

Highlights

Physics-informed neural networks for parameter learning of wildfire spreading

K. Vogiatzoglou, C. Papadimitriou, V. Bontozoglou, K. Ampountolas

- An interpretable wildfire model seamlessly provides robust data-driven capabilities.
- A concise set of key model parameters enables learning via deep neural networks.
- PiNNs integrate a training dataset while satisfying wildfire system dynamics.
- Efficacy of PiNNs in 1D and 2D fire fronts employing synthetic data.

Physics-informed neural networks for parameter learning of wildfire spreading

K. Vogiatzoglou^{a,*}, C. Papadimitriou^a, V. Bontozoglou^b and K. Ampountolas^c

^aSystem Dynamics Laboratory, Department of Mechanical Engineering, University of Thessaly, Volos, 38334, Greece

^bTransport Processes & Process Equipment Laboratory, Department of Mechanical Engineering, University of Thessaly, Volos, 38334, Greece

^cAutomatic Control & Autonomous Systems Laboratory, Department of Mechanical Engineering, University of Thessaly, Volos, 38334, Greece

ARTICLE INFO

Keywords:

Wildfire spreading
Physical model
Parameter learning
Deep learning
Physics-informed neural network
Physics-informed digital twin

ABSTRACT

Wildland fires pose terrifying natural hazards, underscoring the urgent need to develop data-driven and physics-informed digital twins for wildfire prevention, monitoring, intervention, and response. In this direction of research, this work introduces a physics-informed neural network (PiNN) to learn the unknown parameters of an interpretable wildfire spreading model. The considered wildfire spreading model integrates fundamental physical laws articulated by key model parameters, essential for capturing the complex behavior of wildfires. The proposed machine learning approach leverages the theory of artificial neural networks with the physical constraints governing wildfire dynamics, such as the first principles of mass and energy conservation. Training of the PiNN for physics-informed parameter identification is realized using data of the temporal evolution of one- and two-dimensional (plane surface) fire fronts that have been obtained from a high-fidelity simulator of the wildfire spreading model under consideration. The parameter learning results demonstrate the remarkable predictive ability of the proposed PiNN in uncovering the unknown coefficients in both the one- and two-dimensional fire spreading scenarios. Additionally, this methodology exhibits robustness by identifying the same parameters in the presence of noisy data. The proposed framework is envisioned to be incorporated in a physics-informed digital twin for intelligent wildfire management and risk assessment.

1. Introduction

Wildland fires represent instances of aggressive fire expansion with a profound impact on shaping the characteristics of biotic ecosystems. While they foster the natural survival of various life forms through nutrient cycling, habitat diversity, and seed germination, they also lead to disproportionate implications across multiple facets of living entities in both social, economic, and environmental domains [1, 2] due to their extreme progression rates. The climate crisis, exacerbated by greenhouse gas effects, global warming, and water scarcity, along with detrimental human interventions, including unfavorable land use at the wildland-urban interface (WUI) and increased forest flammability, highlight wildfires as an exceedingly frequent and severe disaster, confined to a finite set of trustworthy simulation software capable of predicting their spread.

The primary focus of a holistic simulation tool should always prioritize human safety and the preservation of natural viability. As a very complex phenomenon, fire behavior models aim to anticipate the direction and intensity of fire spread rates by blending historical (offline) data with continuously evolving geospatial and environmental (online)

*Corresponding author

✉ kvogiatzoglou@uth.gr (K. Vogiatzoglou); costasp@uth.gr (C. Papadimitriou); bont@uth.gr (V. Bontozoglou); k.ampountolas@uth.gr (K. Ampountolas)
ORCID(s): 0000-0001-6517-8369 (K. Ampountolas)

data sources. However, the acquisition of online data during fire propagation presents significant challenges, such as sparsity and costliness. Thus, the incorporation of synthetic data generated by well-designed simulation models is essential. Despite significant efforts to develop a unified digital tool to interpret the multifaceted dynamics involved [3–5], the extreme threat posed by wildfires remains an ongoing issue within the field of natural science. Accordingly, there is a growing demand for a deeper understanding of the core principles governing these natural processes [6].

Fire experts recognize that in emergent situations, empirical (including statistical) models are the most operationally oriented approaches, as they provide promptly information about the rate of spread (ROS) and direction of the fire front without requiring any detailed theoretical background [4, 7, 8]. Due to their "rule-of-thumb" nature, these models instantly leverage measurements of the ongoing fire event (and/or historical fires) to provide generalized recommendations concerning coordination, evacuation, and suppression [9, 10]. Even so, their applicability falls short during extreme-danger operating conditions (e.g., spotting-moving fires, propagation over undulating terrain, and steep slopes), and they fail to represent the full functional range under constant environmental variations. Conversely, and according to our envisioned modeling approach [11], physics-based formulations appear to compactly integrate fundamental aspects of fluid mechanics, heat transport, and reaction kinetics theory [12–15] in an attempt to reflect the actual behavior of a forest fire. Their primary purpose entails the interpretation of the physics behind fire spread and the identification of combustion-driven effects and pyroconvective interactions [16]. In this regard, the developed modeling approach employs computationally efficient methods while delivering faster-than-real-time simulations of wildfire spread with high accuracy [11, 17]. However, the fidelity of these predictions relies on examining the inherent randomness present due to modeling assumptions and data misinformation. Uncertainty quantification is essential for reducing both aleatoric (i.e., noisy data) and epistemic (i.e., scattered and limited data) uncertainties. At the other end of the spectrum, computational fluid dynamics (CFD) simulations represent the third modeling category, encompassing all spatial and temporal scales while allowing the interaction of fuel, fire, and atmosphere [18–20]. These models offer high-resolution, three-dimensional simulations (wildfire spreading solver) under dynamic weather conditions and complex terrain features, although they necessitate extended memory allocation and computing power. Furthermore, they can capture both the updraft movement of plume (atmospheric boundary-layer solver) [21] and provide detailed insights into the combustion process (combustion solver) [22].

Generally, the management of wildfires imposes advanced predictive resources within a physics-constrained and data-driven simulation software [14]. This innovative modeling approach acts as the centerpiece of a comprehensive digital tool, facilitating coordination among communities by delivering immediate responses within a hazard and risk assessment framework. However, prediction accuracy is hindered by uncertainties stemming from both the model derivation (physical and chemical abstractions) and the incorporation of noisy data. To address these challenges, it's imperative to integrate instantaneous measurements of acceptable precision, acquired through remote sensing

methods (e.g., satellite, drone, and weather radar strategies [23]), into the simulation workflow. A data-informed wildfire decision support system should seamlessly combine the power of fast predictive execution with the benefits of a physics-based formulation, enabling accurate forward estimations within an efficient parameter learning approach [11], thus further strengthening the overall proactive and responsive tactics under real-time limitations.

Among the preceding assumptions, parameter learning emerges as a notable enhancement toward acquiring a more profound insight into this ecological challenge. Numerous literature reviews emphasize the necessity of incorporating both synthetic [24] and real data [25, 26] using diverse methodologies for parameter identification [27–29]. Empirical correlations combined with level-set methods [30, 31] have been proposed for model calibration, collecting measurements from the fire front shape, wind flow, and fuel properties. These approaches minimize a least-squares objective function that quantifies the difference between simulated and observed data at multiple time instants. Ensemble Kalman filtering [14, 17, 32], along with Monte Carlo simulations [33], have been suggested to include uncertainties in both measurements and predictions, update vital model parameters, and deliver data-driven wildfire forward estimations. Nonetheless, these methods struggle to accommodate noisy data and are restricted due to dimensionality constraints, highlighting the requirement for a more cohesive methodology.

Under the concept of these limitations, a novel framework of inverse optimization algorithms has emerged, known as physics-informed neural networks (PiNNs) [34–37], amplifying the range of conventional parameter learning methods. Building on this, the present work aims to apply and demonstrate the effectiveness of PiNNs specifically for learning the parameters of a wildfire spreading model [11]. PiNNs represent data-driven machine learning approaches that merge the theory of artificial neural networks (ANNs) with the physical constraints of real-world systems, restricting the range of possible model solutions. This integration represents the first contribution in the literature to the learning process of the unknown (hard to assess) model parameters that capture essential physical and chemical properties of the fire front. The proposed methodology for physics-informed parameter identification of a wildfire spreading model includes two fundamental constituents: (i) an artificial neural network, also recognized as a universal approximator [38], parameterized by weights and biases; and (ii) the adherence to the physical laws of the dynamical wildfire spreading model [11], as described by ordinary or partial differential equations (ODEs, PDEs) [35]. Effective training of PiNNs requires robust data acquisition methods to generate an adequate training dataset, considering both the size and quality of the data points. To this end, the developed PiNN is trained using wildfire spreading data that have been obtained from a high-fidelity simulator of the system under consideration. As for the modeling formulation, it is grounded in the first principles of mass and energy conservation, while synthetic data regarding temperature and fuel measurements are incorporated into the training phase. This enables the network to systematically explore the full range of feasible parameters and ultimately converge to their nominal values.

The remainder of this paper is structured as follows. Section 2 provides a concise overview of the wildfire model derivation and delineates the essential model parameters for learning. Section 3 introduces the streamline configuration of PiNNs and details the overall training process. Section 4 outlines some significant case studies, focusing on validating the effectiveness of PiNNs. Finally, Section 5 presents conclusions drawn and offers suggestions for future enhancements.

Notation: The set of real numbers is denoted by \mathbb{R} . The dot product operator between two vectors $\mathbf{a} = [a_1 \ a_2]^T$ and $\mathbf{b} = [b_1 \ b_2]^T$ is represented by $\langle \cdot \rangle$, and yields $\mathbf{a} \cdot \mathbf{b} = a_1 b_1 + a_2 b_2$. The gradient operator ∇_{xy} is expressed as $\nabla_{xy} = \frac{\partial}{\partial x} \hat{i} + \frac{\partial}{\partial y} \hat{j}$, where \hat{i} and \hat{j} represent the unit vectors in the x - and y -directions, respectively. Moreover, $\nabla_{xy}^2 = \frac{\partial^2}{\partial x^2} + \frac{\partial^2}{\partial y^2}$ stands for the Laplace operator. Eventually, when f_i is mentioned, it indicates the derivative of the state variable f with respect to i . Similarly, f_{ii} denotes the second derivative of f with respect to i . State variables for the considered wildfire model include the temperature T , the endothermic fuel E , and the exothermic fuel X .

2. Wildfire spreading modeling

This section briefly presents an interpretable physics-based wildfire model to emulate wildfire expansion and its crucial model parameters for physics-informed parameter identification [11].

2.1. Model formulation

Wildfire modeling necessitates the incorporation of diverse spatiotemporal scales and natural processes, alongside the intricate chemistry of burning fuel and the detailed physics governing fluid flow and heat transport [3, 39]. In this streamlined modeling approach, the reaction kinetics include Arrhenius expressions for water dehydration and wood combustion. Heat transfer is modeled by a combination of both radiation, convection, and dispersion (conduction) [5, 16]. These mechanisms attempt to describe the complex physical phenomena induced by the interaction of airflow fluctuations above and within the plantation and buoyant flame instabilities [40]. Moreover, specific topographical features may result in zones dominated by chaotic turbulent vortices (turbulent diffusion) generated by flame buoyant forces [41, 42], which strongly affect the direction and intensity of the ongoing wildfire event by creating updrafts (bursts) and downdrafts (sweeps) flame movements.

The burning fuel is considered a solid material composed of two elements: water and combustibles [22, 43]. Specifically, the mass fraction of water, denoted as E , encompasses the internal content of the plant (live humidity) and the water condensed on the plant (dead humidity). The remaining mass fraction of combustibles, denoted as X , comprises both volatiles (e.g., CO, CO₂, NO_x, and VOC) and charcoal. Following a fundamental framework, combustion initiates with water evaporation (as the endothermic phase), progresses through volatilization and charring reactions, and ultimately terminates with oxidation reactions (as the ensuing exothermic phase) [44, 45]. Thus, the

endothermic (gaseous) part of the combustion process is modeled using the Arrhenius kinetics formulation as:

$$r_e = c_1 e^{-\frac{b_1}{T}}. \quad (1)$$

The same equation is applied to the exothermic (solid) phase of the combustion process. However, the possible shortage of oxygen modifies the total exothermic reaction term [46], leading to:

$$r_x = \frac{c_2 e^{-\frac{b_2}{T}} r_o}{c_2 e^{-\frac{b_2}{T}} + r_o}, \quad (2)$$

where T ([=] K) represents the temperature of the fire layer, c_1, c_2 ([=] s⁻¹), along with b_1, b_2 ([=] K), signify crucial parameters of the ignition and combustion process. Additionally, r_o ([=] s⁻¹) embodies the presence or absence of oxygen (frequency of incoming oxygen) during the pyrolysis stage.

The proposed model implements a novel method to separate the thermal energy from the fluid mechanics component (momentum conservation) and facilitates simplified versions of combustion kinetics by focusing on key reaction pathways and mass-energy balances to deliver insights into temperature dynamics and fuel composition effects. It employs a computationally inexpensive system of differential equations, which empowers simple calculations while maintaining acceptable accuracy [13–16]. Additionally, this straightforward approach incorporates fundamental physics articulated by a finite set of key model parameters, making it adaptable to sensory input data [23, 47], as well as enabling data-informed estimations. These advancements contribute to the development of a compact physics-based system in the form of (see [11] for details):

$$\frac{\partial T}{\partial t} = \alpha_1 \left(\underbrace{\mathbf{D}\nabla_{xy}^2 T}_{\text{dispersion}} - \underbrace{\mathbf{u} \cdot \nabla_{xy} T}_{\text{advection}} \right) - \underbrace{\alpha_2 E r_e + \alpha_3 X r_x}_{\text{reaction}} - \underbrace{\alpha_4 U (T - T_a)}_{\text{convection}}, \quad (3)$$

$$\frac{\partial E}{\partial t} = -E r_e, \quad (4)$$

$$\frac{\partial X}{\partial t} = -X r_x, \quad (5)$$

where T symbolizes once more the temperature of the fire layer, E the endothermic fuel, and X the exothermic fuel. The coefficients $\alpha_1, \alpha_2, \alpha_3$, and α_4 represent fuel, combustion, and environmental properties, while the notation T_a ([=] K) denotes the ambient temperature, $\mathbf{D} = [D_x \ D_y]^T$ ([=] m²/s) is the dispersion coefficient vector, $\mathbf{u} = [u_x \ u_y]^T$ ([=] m/s) is the velocity vector replicating gas flow averaged over the plantation height, and U ([=] W/m²K) is the overall heat transfer coefficient governing thermal losses to the environment.

2.2. Parameter learning

The spread of forest fires is driven by highly non-linear natural events, influenced by numerous dynamically competitive subprocesses and multi-physics phenomena that appear to affect the intensity and direction of combustion fronts. The envisioned physics-based model employs a straightforward mathematical concept to sufficiently simulate wildfire expansion, relying on a limited set of crucial model parameters. Therefore, within the context of parameter inference, this work aims to elucidate the substantial impact of \mathbf{D} , \mathbf{u} , and U parameters, compactly represented as $\theta = [\mathbf{D}^\top \mathbf{u}^\top U]^\top$, on the rate of fire front spread [12, 48].

It is generally accepted in the literature that, under different prevailing weather conditions, radiation or convection have a dominant effect on the shape of the flame front and its spreading characteristics [6]. While convection tends to dominate wind-driven propagation (eruptive fires) by advancing the hot combustible gases directly to the unburned fuel, radiation primarily enhances the immediate preheating and ignition of fuel (plume-dominated fires) [16]. The dispersion coefficient \mathbf{D} of the present model integrates the combined effects of radiation, buoyant instabilities, and turbulent streamwise vortices. As an uncertain model parameter, it also depends on the dynamic fluctuation of the mean gaseous velocity [42] and the characteristic length scales of the fire front. Specifically, this coefficient combines the fire line length [49], measured along the flame axis, and the fire line width [50], measured from the head to the lateral flame parts. A shorter fire line favors more efficient re-direction of wind around the main fire spot, while a longer fire line tends to force wind penetration through the fire front. As a result, the fire front spreads faster forward and also extends progressively in the lateral direction (creating the well-known parabolic fire front shape) [19, 48]. Thus, this parameter is of profound importance in shaping the fire line geometry and influencing the acceleration or deceleration of the growth and spread rate.

The influence of wind is undeniably pivotal [40, 51], dictating not only the ROS but also the overall propagation dynamics of fire. However, wind measurements remain susceptible to significant variability stemming from abrupt spatial and temporal atmospheric and topographical irregularities [52]. The mean gaseous velocity \mathbf{u} fluctuates between minimum values due to the drag resistance of the foliage and upward plume (vertical wind shear stresses), reaching maximum values when the canopy is diminished by fire spread. Moreover, gas flow affects the dispersion and convection heat terms, determining the magnitude of heat fluxes provided to the ambient system [19]. For the upcoming case studies, the examination will focus on a flat terrain where the gaseous phase moves uniformly over and through the plantation (in space). The primary focus centers on the functionality of the ANN for parameter learning rather than delving into the intricate physics of wind modeling.

The total thermal loss coefficient U holds significant importance as it signifies the extent of heat release to the surroundings. This stochastic term in the physical model accounts for the combined effects of natural convection [53] and radiation [5, 16] and typically constitutes a non-linear function of temperature, as defined by both the Boltzmann

law and the Nusselt correlation (for free convection). When this coefficient increases, heat losses intensify, leading to a passive combustion front and, thus, a halt in fire propagation. On the contrary, lower values enhance the fire field with higher temperature records and intense progression rates.

The aforementioned model parameters appear to be the most appropriate for learning, as they cover a considerable portion of both model and environmental uncertainties, ultimately exerting a profound impact on the dynamics of forest fires. Further details concerning model derivation and parameter descriptions can be found in [11]. To effectively train physics-informed neural networks for inference purposes, the synthetic data used as training sets in Section 4 employs either constant values for these coefficients or values that fluctuate with time in order to account for the effect of model error in the inference process. In the latter case, the fluctuations are considered to be samples of a Gaussian process with a specific correlation structure.

3. Physics-informed neural networks for inverse optimization

3.1. Artificial neural networks

This section briefly describes the architecture of artificial neural networks and their primitive functionality. Consider a fully-connected feed-forward neural network represented by a compositional function, $\mathcal{N}^L(\mathbf{x}) : \mathbb{R}^n \rightarrow \mathbb{R}^m$, of L layers, while N_ℓ indicates the number of artificial neurons at each intermediate (hidden) layer, with $\ell = 1, 2, \dots, L-1$. In terms of the initial (input) layer, $N_0 = n$, reflecting the dimension of the input training data $\mathbf{x} \in \mathbb{R}^n$. In contrast, the final (output) layer has $N_L = m$, determined by the dimension of the output quantities of interest. Commonly, ANNs are tailored for either classification tasks, such as organizing data into specific categories, or regression tasks, like predicting numerical values given a set of training data.

Every neuron's output passes through an activation function, $\sigma(\mathbf{x}) : \mathbb{R}^n \rightarrow \mathbb{R}^n$, which is an operator introducing non-linearity to the network, enabling it to capture intricate patterns present in the training dataset. The activation function transforms the weighted linear sum input of one layer into a non-linear output for the subsequent layer and determines whether a neuron is excited or inhibited. Several activation functions are available, among which the most common are the logistic sigmoid $\sigma(x) = \frac{1}{1+e^{-x}}$, the hyperbolic tangent $\sigma(x) = \tanh(x) = \frac{e^x - e^{-x}}{e^x + e^{-x}}$, and the rectified linear unit (ReLU) $\sigma(x) = \max(x, 0)$, which can be approximated by a smooth differentiable function of the form $\sigma(x) = \ln(1 + e^x)$. In general, activation functions have the property: $-\infty < \lim_{x \rightarrow -\infty} \sigma(x) < \lim_{x \rightarrow \infty} \sigma(x) < \infty$.

A neural network can be understood as a function approximator or surrogate model parameterized by weights, which adjust the strength of connections between neurons of different layers, and biases, which control the flexibility of the network. Let $\mathbf{W}^\ell \in \mathbb{R}^{N_\ell \times N_{\ell-1}}$ and $\mathbf{b}^\ell \in \mathbb{R}^{N_\ell}$ be the weight matrix and bias vector at the ℓ -th layer, where $\ell = 1, 2, \dots, L$, respectively. The primary objective of this approach involves fixing the weights and biases, or the concatenated vector $\mathbf{A} = \{\mathbf{W}^\ell, \mathbf{b}^\ell\}_{1 \leq \ell \leq L}$ to their optimal values, leveraging labeled pairs of input and

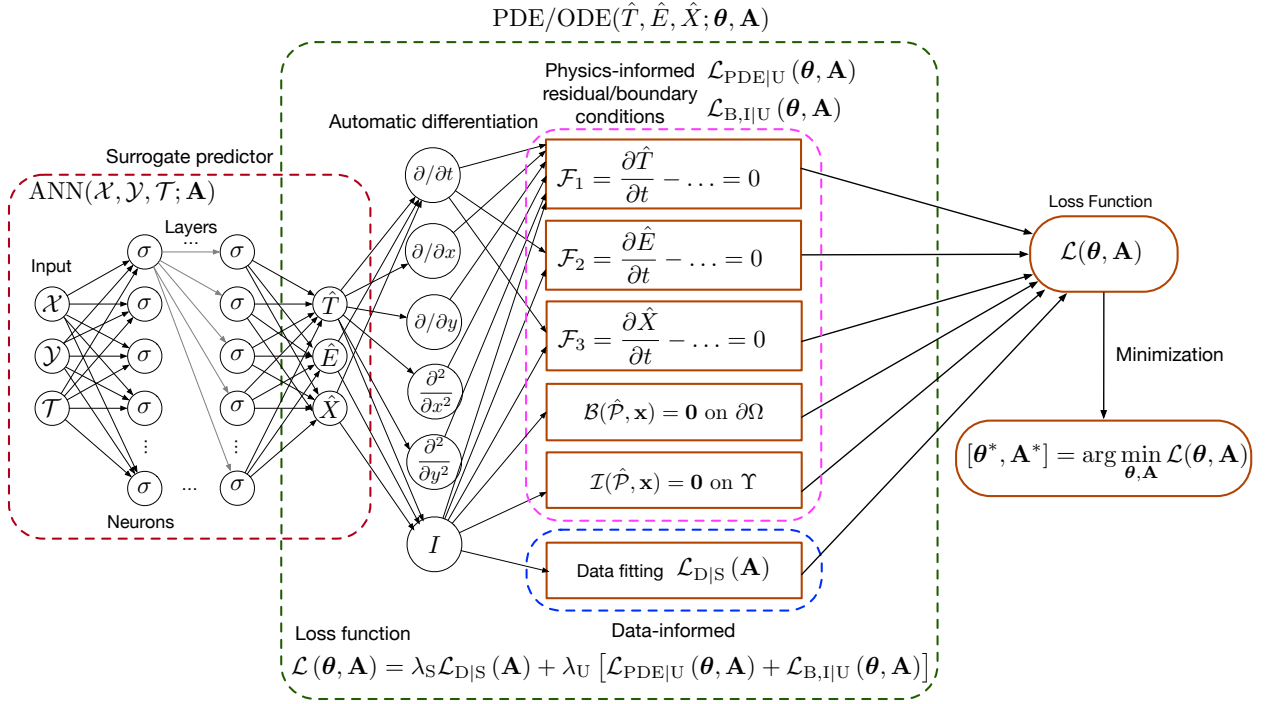


Figure 1: Architecture of the proposed PiNN for learning the parameters of the wildfire spreading model. The ANN on the left represents the physics-uniformed (data-driven) surrogate predictor, while the right network illustrates the physics-informed (data-uniformed though) residual, initial and boundary conditions of the wildfire model, and the data-informed cost function (data fitting) that penalizes deviation of the surrogate model predictions from the synthetic data.

output data (supervised learning). Specifically, the ANN tries to minimize the discrepancy between predicted and target outputs via a loss function and enhance its generalization ability to unseen data. Regarding this, automatic (or algorithmic) differentiation [54] in general and the backpropagation algorithm [55] in particular contribute to the efficient computation of loss gradients with respect to the network parameters. Moreover, for the nonlinear, high-dimensional optimization problem present, gradient-based optimizers and their variants (e.g., stochastic gradient descent (SGD) [56] as well as Adam [57] and L-BFGS [58] algorithms are commonly employed to search for global minima. The architecture stated above can be described as follows (see also the left part of Figure 1):

$$\text{Input layer: } \mathcal{N}^0(\mathbf{x}) = \mathbf{x} \in \mathbb{R}^n, \quad (6)$$

$$\text{Hidden layers: } \mathcal{N}^\ell(\mathbf{x}) = \sigma(\mathbf{W}^\ell \mathcal{N}^{\ell-1}(\mathbf{x}) + \mathbf{b}^\ell) \in \mathbb{R}^{N_\ell} \quad \text{for } \ell = 1, 2, \dots, L-1, \quad (7)$$

$$\text{Output layer: } \mathcal{N}^L(\mathbf{x}) = \mathbf{W}^L \mathcal{N}^{L-1}(\mathbf{x}) + \mathbf{b}^L \in \mathbb{R}^m. \quad (8)$$

The Universal Approximation Theorem (UAT), the most important theoretical result in neural networks (NNs), states that a neural network of the architecture (6)–(8) and a large class of activation functions (including sigmoid and ReLU) can approximate arbitrarily closely (in an appropriate mathematical sense) any piecewise continuous function

provided the number of hidden layers is sufficiently large, showing that universal approximation is essentially implied by the network structure [38, 59–61]. While the UAT provides some assurance about the capability of ANNs to approximate functions to an arbitrary degree of accuracy, it does not provide any rigorous theoretical results on the size of the ANN (in terms of hidden layers and neurons per hidden layer) needed nor its performance. In practice, a trial-and-error procedure can be pursued to obtain an appropriate set of hyperparameters that result in "good" performance (accuracy of approximation). For a more systematic hyperparameter search to tune deep ANNs, Bayesian optimization can be employed, as in AlphaZero [62].

The contribution of PiNNs to high-dimensional contexts governed by parameterized equations has recently surfaced, stepping into both forward (data-driven prediction) and inverse (data-driven discovery) problems with great promises. The integration of PDEs and/or ODEs for regularization purposes by enforcing the physical laws of the dynamic system (prior knowledge) in accordance with the selected training dataset signifies a substantial advancement towards improving the performance of the learning algorithm (accelerated convergence).

3.2. Training of PINNs

Consider the wildfire spreading model (3)–(5), with an explicit solution denoted by $\mathcal{P} \equiv \mathcal{P}(\mathbf{x}) = [T(\mathbf{x}) E(\mathbf{x}) X(\mathbf{x})]^\top$, defined over the spatial domain $\Omega \subset \mathbb{R}^2$, and temporal domain Υ , where $\mathbf{x} \in \Omega \times \Upsilon$ is the input, parameterized by the vector $\boldsymbol{\theta} = [\mathbf{D}^\top \mathbf{u}^\top U]^\top$ (to be learned). The residuals of (3)–(5) are given by:

$$\mathcal{F}_1(T, T_x, T_y, T_{xx}, T_{yy}, \mathcal{P}, \boldsymbol{\theta}) = \frac{\partial T}{\partial t} - \alpha_1 \left(\mathbf{D} \nabla_{xy}^2 T - \mathbf{u} \cdot \nabla_{xy} T \right) + \alpha_2 E r_e - \alpha_3 X r_x + \alpha_4 U (T - T_a) = 0, \quad (9)$$

$$\mathcal{F}_2(E, \mathcal{P}) = \frac{\partial E}{\partial t} + E r_e = 0, \quad (10)$$

$$\mathcal{F}_3(X, \mathcal{P}) = \frac{\partial X}{\partial t} + X r_x = 0. \quad (11)$$

The mathematical system described above is imposed by a set of boundary conditions $\mathcal{B}(\mathcal{P}, \mathbf{x})$ on $\partial\Omega$ and initial conditions $\mathcal{I}(\mathcal{P}, \mathbf{x})$ on Υ , emulating the physics driving fire fronts. Taking advantage of synthetic data $\mathcal{D} = \{\mathcal{P}(\mathbf{x})\}_{\mathbf{x} \in \Omega \times \Upsilon}$ regarding temperature and fuel measurements, the neural network is constrained to generate predictions satisfying both the physical model (eqs. (9)–(11)) and the boundary conditions, $\mathcal{B}(\mathcal{P}, \mathbf{x}) = \mathbf{0}$, as well as the initial conditions, $\mathcal{I}(\mathcal{P}, \mathbf{x}) = \mathbf{0}$.

The input layer incorporates labeled data with specific spatial and temporal sampling frequencies. Spatial points are denoted as $\mathcal{X} = \{x_1, x_2, \dots, x_{|\mathcal{X}|}\}$, $\mathcal{Y} = \{y_1, y_2, \dots, y_{|\mathcal{Y}|}\} \in \Omega$, and temporal points as $\mathcal{T} = \{t_1, t_2, \dots, t_{|\mathcal{T}|}\} \in \Upsilon$, where $|\mathcal{X}|, |\mathcal{Y}|, |\mathcal{T}|$ express the cardinality of sets \mathcal{X}, \mathcal{Y} , and \mathcal{T} , respectively. The selection of the appropriate quantity of input data is paramount, necessitating the inclusion of sufficient points from the boundaries ($\in \partial\Omega$) and initial states ($\in \Upsilon$). During training, the neural network is fed by such input pairs of $\mathcal{X}, \mathcal{Y}, \mathcal{T}$ from the entire training spatiotemporal

set, and by integrating synthetic data $\mathcal{D} = \{\mathcal{P}(\mathbf{x})\}_{\mathbf{x} \in \Omega \times \Upsilon}$ attempts to predict the state variables $\hat{\mathcal{P}} = [\hat{T} \ \hat{E} \ \hat{X}]^\top$. To evaluate the efficiency of the network to match predictions with the target values, a mean squared error (MSE) loss function (L_2 -norm) is employed. This total loss function \mathcal{L} includes three critical components: (i) a supervised (data-driven) cost criterion $\mathcal{L}_{\mathcal{D}|\mathcal{S}}$, determined by measurements \mathcal{P} and predictions $\hat{\mathcal{P}}$, at multiple spatiotemporal points; (ii) an unsupervised loss function $\mathcal{L}_{\text{PDE}|\text{U}}$, for the set of residual PDEs; and (iii) an unsupervised loss function $\mathcal{L}_{\text{B,I}|\text{U}}$, for the boundary (\mathcal{B}) and initial (\mathcal{I}) conditions. Thus, the total loss function is expressed as:

$$\mathcal{L}(\boldsymbol{\theta}, \mathbf{A}) = \lambda_{\mathcal{S}} \mathcal{L}_{\mathcal{D}|\mathcal{S}}(\mathbf{A}) + \lambda_{\text{U}} [\mathcal{L}_{\text{PDE}|\text{U}}(\boldsymbol{\theta}, \mathbf{A}) + \mathcal{L}_{\text{B,I}|\text{U}}(\boldsymbol{\theta}, \mathbf{A})], \quad (12)$$

with,

$$\mathcal{L}_{\mathcal{D}|\mathcal{S}}(\mathbf{A}) = \frac{1}{N_{\mathcal{D}}} \sum_{i=1}^{N_{\mathcal{D}}} \|\mathcal{P} - \hat{\mathcal{P}}\|^2, \quad (13)$$

$$\mathcal{L}_{\text{PDE}|\text{U}}(\boldsymbol{\theta}, \mathbf{A}) = \frac{1}{N_{\text{PDE}}} \sum_{i=1}^{N_{\text{PDE}}} (\|\mathcal{F}_1(\hat{T}_t, \hat{T}_x, \hat{T}_y, \hat{T}_{xx}, \hat{T}_{yy}, \hat{\mathcal{P}}, \boldsymbol{\theta})\|^2 + \|\mathcal{F}_2(\hat{E}_t, \hat{\mathcal{P}})\|^2 + \|\mathcal{F}_3(\hat{X}_t, \hat{\mathcal{P}})\|^2), \quad (14)$$

$$\mathcal{L}_{\text{B,I}|\text{U}}(\boldsymbol{\theta}, \mathbf{A}) = \frac{1}{N_{\text{B,I}}} \sum_{i=1}^{N_{\text{B,I}}} (\|\mathcal{B}(\hat{\mathcal{P}}, \mathbf{x})\|^2 + \|\mathcal{I}(\hat{\mathcal{P}}, \mathbf{x})\|^2), \quad (15)$$

where $\lambda_{\mathcal{S}}$ and λ_{U} are non-negative penalty terms (loss weights) for the supervised and unsupervised loss functions (equal to the value 1.0 in our case studies). The selection of these two penalty terms can be either carried out via a trial-and-error procedure (user-defined) or tuned automatically to speed up convergence. The notations $N_{\mathcal{D}}$, N_{PDE} , and $N_{\text{B,I}}$ correspond to the total number of sampling points for each part of the loss function.

In summary, PiNNs typically consist of: (i) a conventional multi-layer neural network (physics-uninformed predictor); (ii) the residual constraints of the dynamic system (physics-informed part), simultaneously accounting for both boundary and initial conditions; and (iii) a total loss function (data-driven fitting cost criterion). This seamless architecture between these components is illustrated in the right part of Figure 1. The ultimate objective (under the concept of the inverse optimization problem) is to learn the best-fit values for both the unknown model parameters, denoted as $\boldsymbol{\theta}^* = [\mathbf{D}^{*\top} \ \mathbf{u}^{*\top} \ \mathbf{U}^*]^\top$, and the weights and biases, denoted as $\mathbf{A}^* = \{\mathbf{W}^{\ell^*}, \mathbf{b}^{\ell^*}\}_{1 \leq \ell \leq L}$, by minimizing the total loss function (12) during training. This can be formulated as:

$$[\boldsymbol{\theta}^*, \mathbf{A}^*] = \arg \min_{\boldsymbol{\theta}, \mathbf{A}} \mathcal{L}(\boldsymbol{\theta}, \mathbf{A}). \quad (16)$$

The underlying optimization problem is highly non-linear and non-convex within a high-dimensional parameter space, provided that the activation functions in each neuron of the ANN are nonlinear operators. However, it can be readily

solved through algorithmic differentiation and the employment of batch methods, such as SGD, Adam, or L-BFGS, which leverages Hessian information.

4. Application and results

4.1. Parameter learning setup

This section underscores the effectiveness of PiNNs to fine-tune the unknown parameters of the wildfire spreading model (3)–(5). Specifically, four representative case studies are conducted: *Case Study 1* explores the ability of PiNNs in learning the parameters for the spatiotemporal evolution of a one-dimensional (1D) fire front of the wildfire spreading model; *Case Study 2* seeks to train neural networks to adjust the same model parameters to their nominal values while dealing with synthetic noisy data; finally, *Case Study 3* and *Case Study 4* demonstrate the predictive ability of PiNNs in learning the parameters for the spatiotemporal evolution of a two-dimensional (2D) fire front on a plane surface without and with noisy data, respectively.

It is important to emphasize that all case studies are carried out on flat terrain with a uniform fuel composition and consistent wind direction across the domain. Moreover, both the dispersion coefficient \mathbf{D} and the velocity term \mathbf{u} indicate vector quantities with components in both the streamwise x - and spanwise y -directions, respectively. Finally, the wildfire spreading model (3)–(5) has been converted into a dimensionless form throughout the entirety of this paper (as for the efficient functionality of the network), allowing for the utilization of non-dimensional simulated temperature and fuel measurements with respect to the training dataset.

4.2. PiNN for 1D fire front

For both *Case Study 1* (see Section 4.2.1) and *Case Study 2* (see Section 4.2.2), the neural network architecture consists of one (1) input layer containing two (2) neurons, representing the discretized spatiotemporal domain $\in \mathbb{R}^2$ ($x \in \Omega$ for spatial and $t \in \Upsilon$ for temporal coordinates). This is followed by four (4) hidden layers, each with twenty (20) neurons, and finally concludes with one (1) output layer with three (3) neurons, which serve to provide the predicted state variables $\hat{\mathcal{P}} = [\hat{T} \ \hat{E} \ \hat{X}]^\top \in \mathbb{R}^3$. Given the notation for the NN's architecture (see Section 3.1): $L = 5$, $N_0 = 2$, $N_\ell = 20$ for $\ell = 1, 2, 3, 4$, and $N_5 = 3$. Thus, the parameterized set of weights and biases can be expressed as $\mathbf{A} = \{\mathbf{W}^1, \mathbf{W}^2, \mathbf{W}^3, \mathbf{W}^4, \mathbf{W}^5, \mathbf{b}^1, \mathbf{b}^2, \mathbf{b}^3, \mathbf{b}^4, \mathbf{b}^5\} \in \mathbb{R}^{1383}$.

The output of each neuron (in terms of hidden and output layers) undergoes a logistic sigmoid activation function $\sigma(x) = \frac{1}{1+e^{-x}}$, enabling the network's capacity to discern intricate non-linear correlations within the training dataset. To expedite convergence, a hybrid training scheme is adopted. Initially, the Adam algorithm is employed for 40,000 iterations, after which the optimization process transitions to L-BFGS for the remainder of the training. The learning rate is set to 0.0003 to induce smooth updates during the exploration stage. This adjustment is essential for achieving

improved performance and accelerated convergence. The training is conducted on a computer with an AMD Ryzen Threadripper PRO 3995WX at 2.70 GHz and 32 cores, operating on Windows 10 Pro 64-bit.

The wildfire spreading model (3)–(5) is governed by a simple set of boundary and initial conditions. Specifically, at the initial state ($t = 0$ s), the conditions \mathcal{I} are set as follows: $T(x, 0) = T_p e^{-\frac{(x-x_0)^2}{\gamma^2}} + T_a$, $E(x, 0) = E_0$, and $X(x, 0) = X_0 \forall x \in \Omega$. Here, T_p ([=] K) represents an approximation of the pyrolysis temperature, x_0 ([=] m) denotes the spatial coordinate corresponding to the maximum temperature value during the ignition phase, γ ([=] m) signifies the extend of the initial fire spot, and E_0 , X_0 denote the constant compositions of the endothermic and exothermic fuel, respectively. Furthermore, to account for boundaries unaffected by fire progression (satisfactorily extended domain), Dirichlet boundary conditions \mathcal{B} are employed, wherein: $T(0, t) = T(L, t) = T_a$, $E(0, t) = E(L, t) = E_0$, and $X(0, t) = X(L, t) = X_0 \forall t \in \Upsilon$, with L ([=] m) characterizing the total length of the simulated domain.

4.2.1. Parameter learning for 1D fire front with synthetic data

The main focus of *Case Study 1* is to demonstrate the pivotal role of PiNNs in inferring the three unknown physical quantities, D , u , and U (scalar values), within the wildfire spreading model. Synthetic data are meticulously prepared and tested applying known values for the above model parameters, denoted as $\theta^* = [D^* \ u^* \ U^*]^T = [0.41 \ 0.25 \ 0.61]^T$. The data generation process involves explicitly solving the mathematical system of equations (3)–(5) through finite difference numerical methods (i.e., central difference scheme for the discretization of the diffusion term and upwinding scheme for the discretization of the advection term) while ensuring compliance to the prescribed boundary and initial conditions (i.e., generated via a physics-informed digital twin). The simulation covers a horizontal spatial domain of $x \in [0, 100]$ m and a time interval of $t \in [0, 200]$ s, while the training dataset includes points sampled at consecutive uniform intervals of $d_x = 1$ m in space and $d_t = 1$ s in time (equivalent to a frequency of 1 Hz) with a total number of 20.301 data points for each state variable (T, E, X).

The outcomes exemplify the efficacy of a well-employed data-assimilation methodology. The ANN implemented the synthetic data during the training part to approximate the a priori known model parameters θ^* while initializing all the unknown coefficients with the estimate 1.0 (during the first iteration). The predicted values have ultimately converged to their nominal counterparts, yielding $\hat{\theta} = [\hat{D} \ \hat{u} \ \hat{U}]^T = [0.408 \ 0.25 \ 0.61]^T \approx \theta^*$. Figure 2 illustrates the convergence behavior of the unknown model parameters over the total course of training iterations. Notably, coefficients u and U exhibit significant convergence after 20.000 iterations, while the L-BFGS optimizer was instrumental in achieving complete alignment beyond 40.000 iterations. The effectiveness of PiNNs is further demonstrated by their robustness in managing circumstances where dispersion and convection coefficients stepped into negative ranges during the exploration stage. The network exploited the embedded prior knowledge (physical modeling constraints) and adeptly adjusted its “learning direction” towards positive ones.

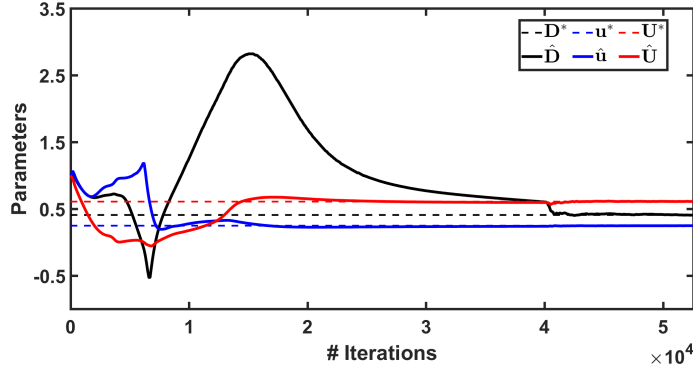


Figure 2: Parameter learning and convergence in the 1D fire front of the wildfire spreading model. The predicted vector of the three model parameters is $\hat{\theta} = [0.408 \ 0.25 \ 0.61]^T$, while the true vector used for generating the training dataset is $\theta^* = [0.41 \ 0.25 \ 0.61]^T$.

With these final estimations, the neural network is calibrated to forecast the entire fire evolution domain across both space (x) and time (t). Figure 3 provides a comparison between the explicit solution (analytically solved) of the physics-based mathematical system and the prediction delivered by PiNNs, demonstrating their ability to accurately replicate the target dataset with minimal expenses in the hidden layer architecture [36]. To enhance clarity, a detailed comparison between the nominal and predicted temperature distributions is conducted at two specific non-dimensional time instants, $t = 0.5$ (intermediate) and 1 (final), for all nodes across the domain. This comparison is delineated in Figure 4, exhibiting the precise alignment between the true and estimated temperature profiles. All these findings demonstrate the substantial predictive capabilities of PiNNs, affirming their effectiveness in accurately forecasting temperature and fuel adjustments over both space and time.

While deep neural networks have resulted in a notable improvement in the spectrum of data-assimilation techniques, questions persist regarding their generalization capabilities. Particularly, concerns arise from the optimal configuration of the network architecture and the necessary number of training data points [63]. Seeking to address these questions, training is conducted with datasets of different magnitudes (more or less data points from the optimal). Specifically, Case 1 (previously described example) includes 20,301 data points, while three new cases, 1A, 1B, and 1C, encompass 80,601, 5,151, and 861 data points for each state variable, respectively. The spatial and temporal sampling frequencies for generating these new training datasets are accordingly: $d_x = 0.5$ m, $d_t = 0.5$ s (for Case 1A), $d_x = 2$ m, $d_t = 2$ s (for Case 1B), and $d_x = 5$ m, $d_t = 5$ s (for Case 1C). Figure 5 demonstrates the sampling distributions of the temperature training datasets between all the examined case studies over the entire spatiotemporal domain. Delving deeper into this, Table 1 clearly illustrates that as the number of sampling points decreases, the accuracy of parameter estimation diminishes. However, even in cases with an insufficient number of data points (see Case 1B and Case 1C), ANN demonstrates promising capability in learning the unspecified parameters, despite experiencing significant oscillations during the training phase. On the other hand, while data can enhance model performance (see Case 1A), it

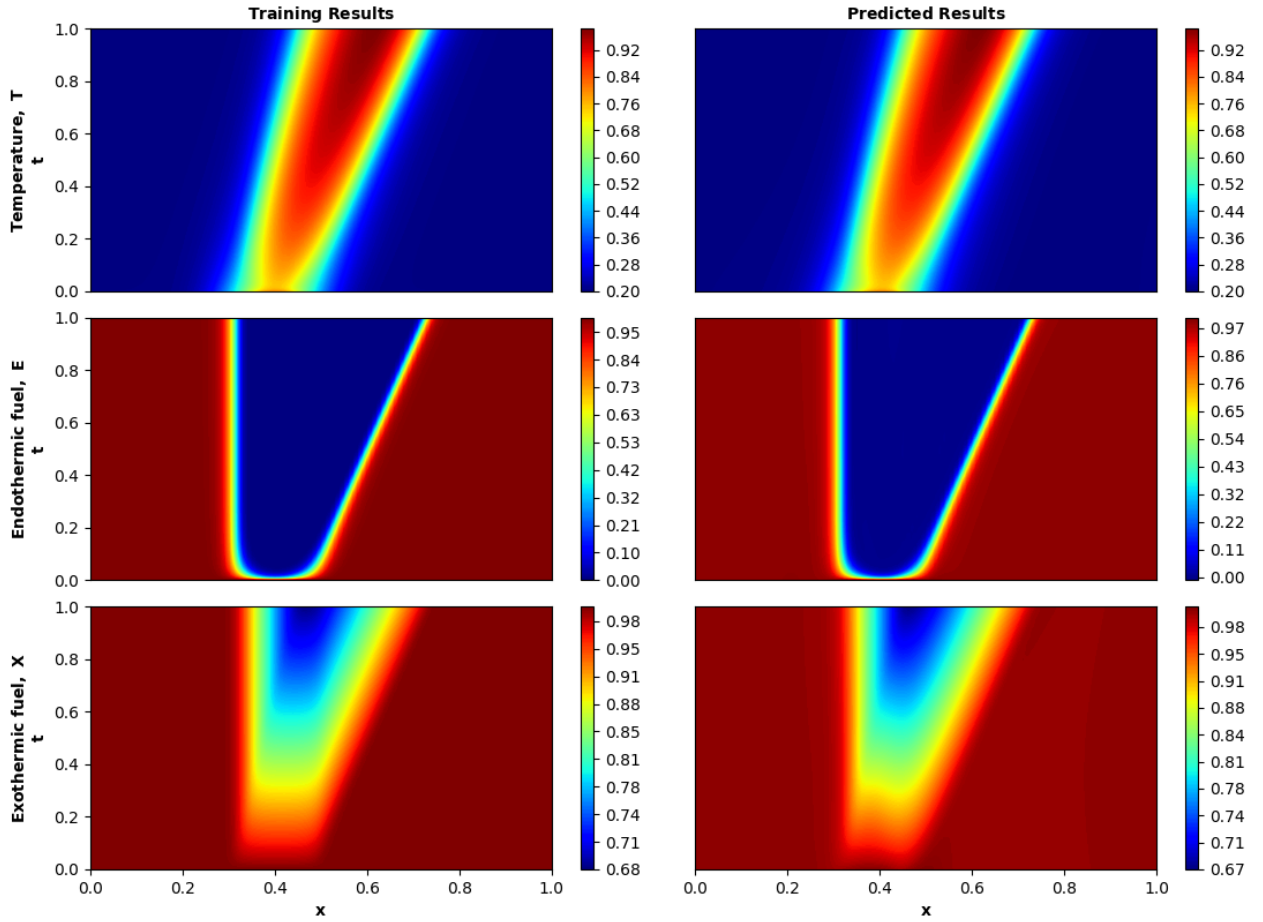


Figure 3: 1D spatiotemporal fire front for the three state variables: T , E , X . The left column presents the explicit solution of the physics-based wildfire spreading model, while the right column displays the prediction of PINNs. Both cases are provided in a dimensionless form.

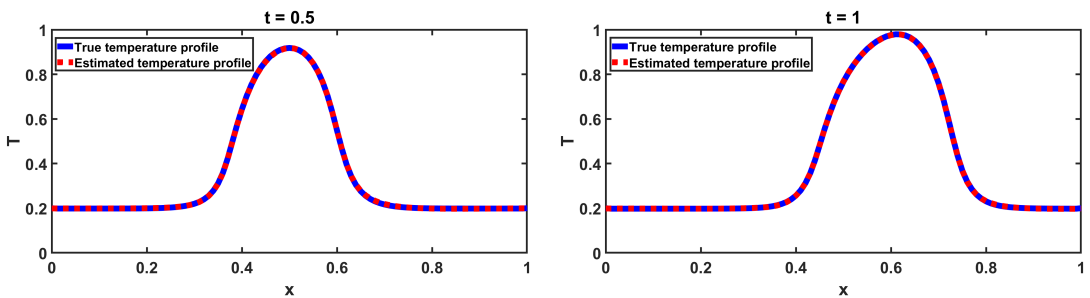


Figure 4: Comparison of the temperature distribution between the explicit solution and the prediction of PiNNs at two specific non-dimensional time instants, $t = 0.5$ and $t = 1$, for all nodes across the spatial fire front.

also has the potential to exacerbate over-fitting issues; therefore, early stopping may offer a solution. The convergence accuracy of Case 1 and Case 1A is ultimately equivalent, thus not requiring a greater amount of data to achieve results with enhanced precision (optimal trade-off between the number of data points and network complexity). In summary,

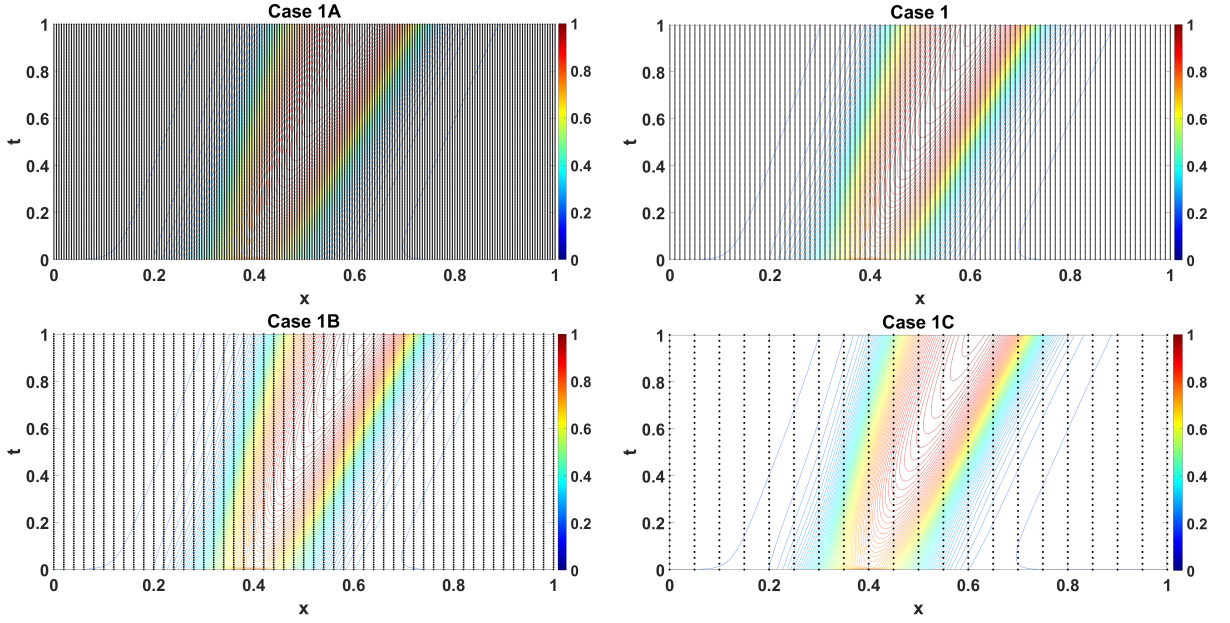


Figure 5: Representation of the training dataset distributions across the temperature profile in both space and time for Case 1 (optimal), 1A, 1B, and 1C. Dot symbols represent the sampling data points used for training in each case.

Table 1

Learning capacity of PiNNs across multiple dataset sizes for Case 1 (optimal), Case 1A, Case 1B, and Case 1C.

Case	Data	d_x ([=] m)	d_t ([=] s)	CPU Time ([=] h)	\hat{D} ([=] m^2/s)	\hat{u} ([=] m/s)	\hat{U} ([=] W/m^2K)
1A	80.601	0.5	0.5	15	0.410	0.250	0.610
1	20.301	1	1	4	0.408	0.250	0.610
1B	5.151	2	2	2	0.471	0.240	0.594
1C	861	5	5	0.5	0.550	0.226	0.573

depending on the nature of the problem and the NN’s architecture, the magnitude (or “density”) of the dataset can be considered one more mutable hyperparameter to tune.

4.2.2. Parameter learning for 1D fire front with synthetic noisy data

As previously mentioned, wildland fires are influenced by a myriad of consecutive biological and chemical processes, and continuous monitoring during an active fire event poses great challenges. Wildfires engender their own micro-climate characteristics (e.g., Pyrocumulonimbus clouds, fire-induced winds, and pyrogenic circulations [3]), introducing randomness into the path of the flames. Measurements are inherently subject to noise due to the instantaneous spatial and temporal variations in both climate conditions (e.g., precipitation rate, wind flow, and moisture content) and thermal degradation processes (e.g., flaming or smoldering-glowing oxidation). While current state-of-the-art fire prediction tools offer numerous simulation software options, they often lack the ability to provide data-driven estimations within the framework of model calibration. Considering that noisy data is the general case

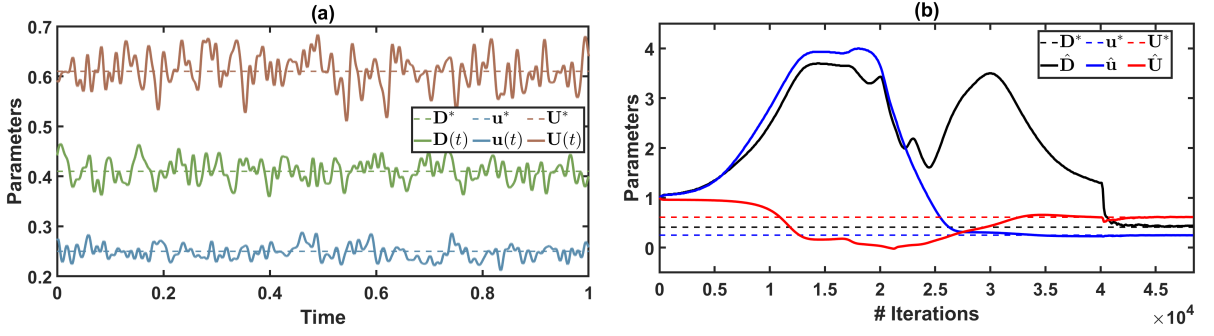


Figure 6: (a) Dotted lines correspond to the constant parameter vector $\theta^* = [0.41 \ 0.25 \ 0.61]^T$ used for generating the training dataset for *Case Study 1*. Solid lines correspond to the temporally perturbed parameter vector $\theta(t) = [D(t) \ u(t) \ U(t)]^T$ employed for generating the training dataset for *Case Study 2*. (b) Parameter learning and convergence process. Predicted vector of the three model parameters, $\hat{\theta} = [0.44 \ 0.242 \ 0.613]^T$. True vector for generating the training data set, $\theta^* = [0.41 \ 0.25 \ 0.61]^T$.

rather than the exception, it is reasonable to investigate the robustness of PiNNs in learning the unknown wildfire spreading model parameters, even under these challenging conditions.

In *Case Study 2*, the formulation and assumptions remain identical to those of *Case Study 1*, with the only exception being the incorporation of simulated training data prepared by introducing noise (model error). Specifically, it is assumed that the parameters $\theta(t) = [D(t) \ u(t) \ U(t)]^T = [D^* + \Delta D(t) \ u^* + \Delta u(t) \ U^* + \Delta U(t)]^T \ \forall t \in \Upsilon$ fluctuate in time around their nominal values $\theta^* = [D^* \ u^* \ U^*]^T = [0.41 \ 0.25 \ 0.61]^T$. Gaussian stochastic processes are used to model these fluctuations $\Delta D(t)$, $\Delta u(t)$, $\Delta U(t)$ with a zero mean and a correlation structure given by $\delta_\varphi^2 e^{-\frac{|t_j - t_i|}{\zeta_\varphi}}$, quantifying the correlation in time. In this context, δ_φ^2 denotes the magnitude of the fluctuations, ζ_φ represents the temporal correlation time, and the subscript φ stands for either the D, u, or U parameter. Specifically, a model error of $\delta_\varphi = 5\%$ and a correlation time of $\zeta_\varphi = 0.005$ is selected, signifying fluctuations around the nominal values θ^* that can reach up to 15%. As our model formulation exhibits functionality at a length scale of hundreds of meters, without addressing the full-scale geophysical problem structure, temporal variations are dominant, thus avoiding capturing possible spatial perturbations. Figure 6(a) provides the comparison between the constant parameter values used in *Case Study 1* and the fluctuated values employed in this example to generate the training datasets.

The outcomes are highly promising, with PiNNs facilitating the convergence of the unknown parameters to their nominal values θ^* , absorbing the substantial fluctuations present in the training dataset. However, due to the appearance of external noise, the network explores a broader range of feasible parameter values, resulting in delayed total convergence, typically observed after 35,000 iterations. Figure 6(b) depicts the obtained results on the learning trajectories of the unknown parameters, successfully converging to $\hat{\theta} = [\hat{D} \ \hat{u} \ \hat{U}]^T = [0.44 \ 0.242 \ 0.613]^T \approx \theta^*$. This resilience exemplifies a significant benefit of PiNNs in handling noisy data (as observed in real-world measurements) [64] compared to traditional data-assimilation methods with restricted tolerance to noise.

4.3. PiNN for 2D fire front

The preceding case studies highlight the importance of PiNNs in the case of 1D wildfire propagation for simplifying complex dynamics, enabling faster computation and easier analysis of fundamental spread mechanisms. While sophisticated three-dimensional (3D) simulation software includes both multi-phase combustion models (operating at centimeter scales) [22], wildfire simulation models (operating at meter scales) [18], and atmospheric boundary layer models (operating at kilometer scales) [20], their practical applicability is limited by the considerable theoretical expertise and high-performance computing resources needed. Consequently, these software solutions are confined only to research settings. In contrast, the 2D modeling of the fire front presented herein serves as the solution for a time-constrained, physics-and-data-informed digital tool capable of incorporating measurements from both ground and airborne sensing platforms (e.g., IR imager data). This tool can instantly inform decision-making authorities to facilitate coordination and aggressive suppression tactics, such as evacuation paths, reforestation policies, and fuel breaks, to mitigate wildfire spread, particularly during emergency situations where firefighting efforts risk being overwhelmed.

In both *Case Study 3* (see Section 4.3.1) and *Case Study 4* (see Section 4.3.2), the focus lies on the precise estimation of the unspecified parameters within the 2D wildfire spreading model. The formulation mirrors the assumptions employed in the 1D scenario, ensuring consistency with the fundamental physics involved. Identical initial and boundary conditions persist (yet extended in two dimensions), considering that boundaries remain unaffected by fire progression. Figure 7 depicts the prototype simulation used to generate the training sample utilized during the execution of the learning algorithm. Each row in the figure represents the evolution of temperature T , endothermic fuel E , and exothermic fuel X , while columns correspond to three specific non-dimensional time instants, $t = 0, 0.5$, and 1 , respectively, captured during the simulation. The depicted figures validate the state-of-the-art fire front geometry, resampling a parabolic shape (horseshoe geometry associated with free-burning fires) characterized by increased forward and intermediate lateral expansion alongside decelerated backward flow [11].

As for the selected neural network architecture, it is similar to that of the 1D modeling formulation, with the notation set as follows: $L = 5$, $N_0 = 3$, $N_\ell = 20$ for $\ell = 1, 2, 3, 4$, and $N_5 = 3$. Specifically, the network includes one (1) input layer with three (3) neurons $\in \mathbb{R}^3$ (representing spatiotemporal coordinates $x, y \in \Omega$ and $t \in \Upsilon$), four (4) hidden layers with twenty (20) neurons each, and one (1) output layer with three (3) neurons $\in \mathbb{R}^3$, corresponding to the predicted state variables $\hat{\mathcal{P}} = [\hat{T} \ \hat{E} \ \hat{X}]^\top$ (same output quantities of interest). Therefore, the parameterized set notation for this network example reads $\mathbf{A} = \{\mathbf{W}^1, \mathbf{W}^2, \mathbf{W}^3, \mathbf{W}^4, \mathbf{W}^5, \mathbf{b}^1, \mathbf{b}^2, \mathbf{b}^3, \mathbf{b}^4, \mathbf{b}^5\} \in \mathbb{R}^{1403}$. Regarding the activation function and optimization algorithms employed, a logistic sigmoid function as well as the Adam algorithm with a learning rate equal to 0.0003 are initially applied for 60.000 iterations, followed by the L-BFGS optimizer to expedite convergence.

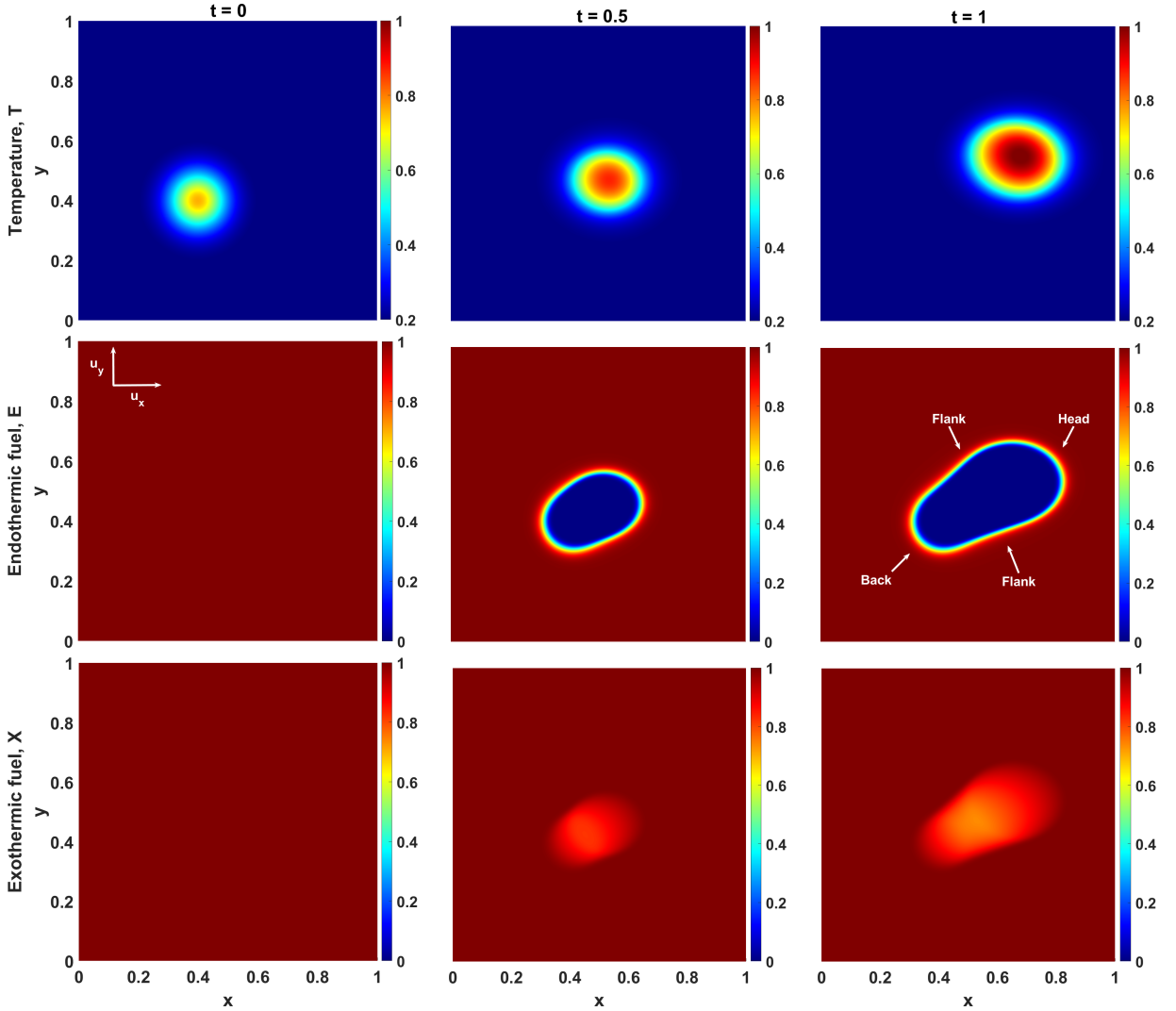


Figure 7: Prototype simulation for the 2D spatiotemporal fire front generated by the wildfire spreading model. Each row represents the state profile of temperature T , endothermic fuel E , and exothermic fuel X . The columns denote the three time instants, $t = 0, 0.5$, and 1 . The results are provided in a dimensionless form.

4.3.1. Parameter learning for 2D fire front with synthetic data

Considering the problem in two dimensions, the diffusion coefficient \mathbf{D} and the mean gaseous velocity \mathbf{u} necessitate two components each in the x - and y -directions, resulting in a total of five model parameters for learning. Once again, synthetic data is generated using the same discretization numerical methods and tested with known predefined values $\theta^* = [D_x^* \ D_y^* \ u_x^* \ u_y^* \ U^*]^T = [0.74 \ 0.41 \ 0.35 \ 0.2 \ 0.4]^T$. The simulation encompasses a rectangular spatial domain of $x \in [0, 100]$ m (streamwise direction), $y \in [0, 100]$ m (spanwise direction), and a time interval of $t \in [0, 200]$ s, while the training dataset comprises simulated points sampled at uniform intervals of $d_x = 4$ m, $d_y = 4$ m in space, and $d_t = 4$ s in time, contributing to a total of 34,476 training points for each state variable. This dataset size has been

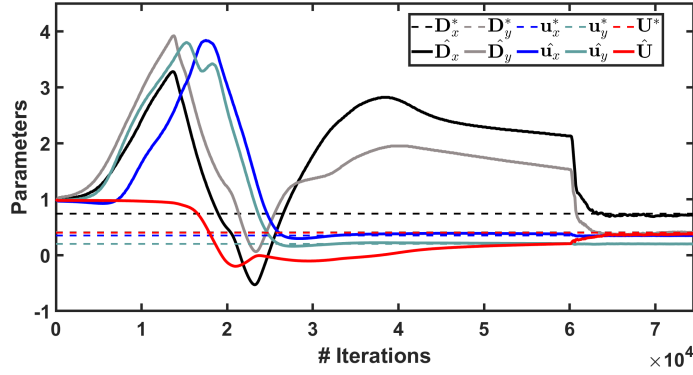


Figure 8: Parameter learning and convergence in the 2D fire front of the wildfire spreading model. The predicted vector of the five unknown model parameters is $\hat{\theta} = [0.724 \ 0.41 \ 0.35 \ 0.2 \ 0.382]^T$, while the true vector utilized for generating the training dataset is $\theta^* = [0.74 \ 0.41 \ 0.35 \ 0.2 \ 0.4]^T$.

found to be optimal, striking a compromise between having sufficient points for training and minimizing architecture complexity.

By initializing all unknown model parameters to the predefined value 1.0 (as an initial guess), PiNNs exhibit rapid convergence towards their nominal values θ^* upon completion of the total number of training iterations (11 h of CPU time). Specifically, as illustrated in Figure 8, certain model parameters (u_x, u_y) reached their nominal values before 30,000 iterations, while the remaining parameters (D_x, D_y, U) required additional steps to achieve complete alignment. The L-BFGS algorithm, taking advantage of the Hessian matrix, accelerated the convergence rate (particularly for the three sensitive parameters) following the completion of the Adam algorithm. This enhancement contributed to the final prediction $\hat{\theta} = [\hat{D}_x \ \hat{D}_y \ \hat{u}_x \ \hat{u}_y \ \hat{U}]^T = [0.724 \ 0.41 \ 0.35 \ 0.2 \ 0.382]^T \approx \theta^*$. PiNNs explored the feasible parameter range and facilitated the transition of specific parameters from negative to positive values.

Finally, the outcomes demonstrate enhanced accuracy, being evident by comparing the temperature distribution between the predictions generated by PiNNs and the explicit solution derived from the mathematical system. In particular, Figure 9 illustrates the temperature profile across the entire domain, examining the differences between the analytical and estimated solution for all nodes in the streamwise x -direction. This evaluation is performed for nodes with a fixed spanwise y -coordinate equal to 0.52 and for two distinct time instants, $t = 0.5$ and 1. The curves are almost identical, signifying a similar spatiotemporal evolution of the fire front. All the consistent robustness across various PiNN operations carries significant implications, as it enables the tackling of more intricate problems across a broader range of dimensions.

4.3.2. Parameter learning for 2D fire front with synthetic noisy data

To assess once more the performance of PiNNs across their entire range of functional capabilities, a brief example employing simulated noisy data is conducted. The ANN architecture and training properties align with the assumptions

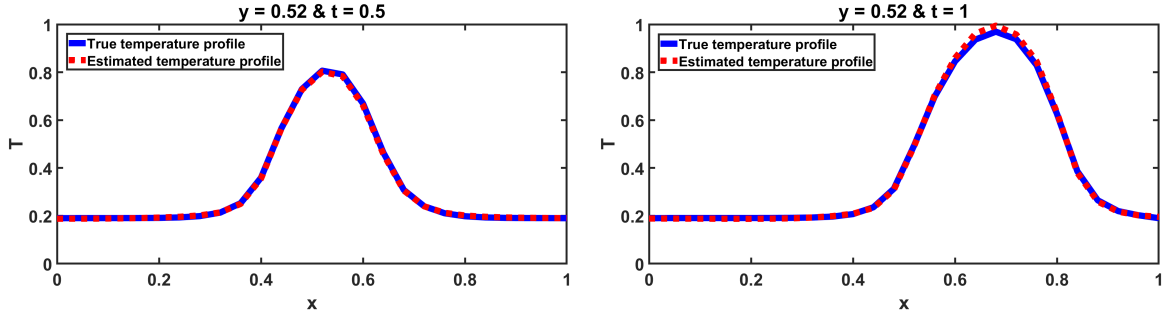


Figure 9: Comparison of the temperature evolution between the explicit solution and PiNNs prediction at two non-dimensional time instants, $t = 0.5$, and $t = 1$, for all nodes across the x domain with $y = 0.52$.

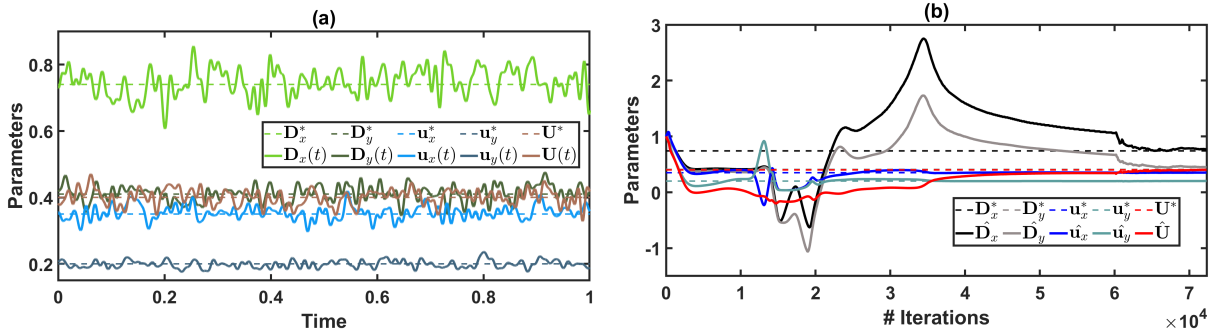


Figure 10: (a) Dotted lines represent the constant parameter vector $\theta^* = [0.74 \ 0.41 \ 0.35 \ 0.2 \ 0.4]^T$, utilized for generating the training dataset for Case Study 3. Solid lines correspond to the temporally perturbed parameter vector $\theta(t) = [D_x(t) \ D_y(t) \ u_x(t) \ u_y(t) \ U(t)]^T$, employed for generating the training dataset for Case Study 4. (b) Parameter learning and convergence process. Predicted vector for the five model parameters, $\hat{\theta} = [0.771 \ 0.449 \ 0.351 \ 0.2 \ 0.4]^T$. True vector used for generating the training dataset, $\theta^* = [0.74 \ 0.41 \ 0.35 \ 0.2 \ 0.4]^T$.

delineated in Section 4.3.1, with the sole modification being the inclusion of training data points perturbed by some form of noise (as further elaborated in Section 4.2.2). A model error equivalent to $\delta_\varphi = 5\%$ and a correlation time of $\zeta_\varphi = 0.005$ are intentionally chosen to introduce temporal fluctuations of approximately 15% around the nominal values $\theta^* = [D_x^* \ D_y^* \ u_x^* \ u_y^* \ U^*]^T = [0.74 \ 0.41 \ 0.35 \ 0.2 \ 0.4]^T$ constituting a vector $\theta(t) = [D_x(t) \ D_y(t) \ u_x(t) \ u_y(t) \ U(t)]^T = [D_x^* + \Delta D_x(t) \ D_y^* + \Delta D_y(t) \ u_x^* + \Delta u_x(t) \ u_y^* + \Delta u_y(t) \ U^* + \Delta U(t)]^T$. This variability is depicted in Figure 10(a), expressing temporal fluctuations around the average values throughout the simulation duration. The remarkable proficiency of PiNNs in learning the unspecified coefficients is evident in Figure 10(b), where the predicted parameter vector $\hat{\theta} = [\hat{D}_x \ \hat{D}_y \ \hat{u}_x \ \hat{u}_y \ \hat{U}]^T = [0.771 \ 0.449 \ 0.351 \ 0.2 \ 0.4]^T$ approximately matches θ^* . This validation, supported by the convergence of the model parameters to their nominal values, underscores the potential of PiNNs as a powerful tool for modeling complex physical systems with inherent noise and randomness.

5. Discussion and conclusions

Wildfire-related natural disasters are among the most intricate environmental phenomena to model, as they initiate complex physical processes while being subject to dynamically evolving atmospheric conditions. The modeling formulation and ambient variations introduce numerous uncertainties, enhancing the risk of inadequate wildfire spreading predictions. This paper demonstrated the importance of PiNNs (with perspectives on data-driven modeling) for estimating some significant unknown wildfire model parameters that are most of the time unavailable to be measured in real-world scenarios. The innovative part centers on restricting the learning process to obey the physical constraints of the dynamic system directly into the training phase, thereby capturing the physics underlying it.

All the examined case studies showcased the utility of PiNNs in uncovering the unknown model parameters across a wide spectrum of representative examples, encompassing both one- and two-dimensional fire front propagation events. Particularly, PiNNs unveiled great efficiency in identifying nominal values based on synthetic data derived from temperature and fuel measurements. Despite the physics-consistent nature of the model, the simplicity of the ANN architecture aligned well with the size of the training dataset. Moreover, this revolutionary approach proved to be functional even when dealing with noisy data. The findings underscore the versatility and operability of PiNNs in addressing complex modeling tasks and boosting their performance not only as inverse but also as forward predictors.

Although PiNNs can effectively learn the required wildfire spreading parameters, there are limitations concerning the complexity of the training phase. Therefore, a narrowed spatiotemporal domain ($x, y = 100$ m and $t = 200$ s) was selected to adequately demonstrate the main physical concept and minimize computational demands. Future research will center on incorporating empirical (observational) data from actual wildfire events over a broader lengthscale in an attempt to explore the adaptability of PiNNs in scattered and high-dimensional contexts. Measurements often represent averaged values over specific regions and may not be directly informative for the spatiotemporal description of all network output quantities of interest. Mixed neural networks, consisting of a convolutional neural network (CNN) for processing satellite imagery alongside a PiNN, portray a notable leap in the direction of improving the broader framework for wildfire management within the field of artificial intelligence and machine learning.

CRedit authorship contribution statement

K. Vogiatzoglou: Data Curation, Formal analysis, Software, Validation, Visualization, Writing - Original Draft. **C. Papadimitriou:** Supervision, Writing - Review & Editing. **V. Bontozoglou:** Methodology, Writing - Review & Editing. **K. Ampountolas:** Conceptualization, Methodology, Project Administration, Visualization, Writing - Review & Editing.

References

- [1] N. Elhami-Khorasani, H. Ebrahimian, L. Buja, S. L. Cutter, B. Kosovic, N. Lareau, B. J. Meacham, E. Rowell, E. Taciroglu, M. P. Thompson, A. C. Watts, Conceptualizing a probabilistic risk and loss assessment framework for wildfires, *Natural Hazards* 114 (2022) 1153–1169.
- [2] A. Carvalho, A. Monteiro, M. Flannigan, S. Solman, A. I. Miranda, C. Borrego, Forest fires in a changing climate and their impacts on air quality, *Atmospheric Environment* 45 (31) (2011) 5545–5553.
- [3] K. Speer, S. Goodrick, *Wildland Fire Dynamics*, 1st Edition, Cambridge University Press, Cambridge, U.K., 2022.
- [4] E. Pastor, L. Zárte, E. Planas, J. Arnaldos, Mathematical models and calculation systems for the study of wildland fire behaviour, *Progress in Energy and Combustion Science* 29 (2) (2003) 139–153.
- [5] M. A. Finney, J. D. Cohen, S. S. McAllister, W. M. Jolly, On the need for a theory of wildland fire spread, *International Journal of Wildland Fire* 22 (1) (2013) 25–36.
- [6] D. Frankman, B. W. Webb, B. W. Butler, D. Jimenez, M. Harrington, The effect of sampling rate on interpretation of the temporal characteristics of radiative and convective heating in wildland flames, *International Journal of Wildland Fire* 22 (2) (2013) 168–173.
- [7] R. C. Rothermel, A mathematical model for predicting fire spread in wildland fuels, U.S. Department of Agriculture, Intermountain Forest and Range Experiment Station (1972) 40.
- [8] E. Marino, J. L. Dupuy, F. Pimont, M. Guijarro, C. Hernando, R. R. Linn, Fuel bulk density and fuel moisture content effects on fire rate of spread: a comparison between FIRETEC model predictions and experimental results in shrub fuels, *Journal Fire Sciences* 30 (4) (2012) 277–299.
- [9] M. G. Cruz, M. E. Alexander, P. M. Fernandes, M. Kilinc, A. Sil, Evaluating the 10% wind speed rule of thumb for estimating a wildfire’s forward rate of spread against an extensive independent set of observations, *Environmental Modelling and Software* 133 (2020) 104818.
- [10] J. A. Vega, P. Cuinas, J. Fonturbel, P. Perez-Gorostiara, C. Fernandez, Predicting fire behaviour in galician (NW Spain) shrubland fuel complexes, *Proc. 3rd International Conference of Forest Fire Research and 14th Conference of Fire Forest Meteorology* 2 (1998) 16–20.
- [11] K. Vogiatzoglou, C. Papadimitriou, K. Ampountolas, M. Chatzimanolakis, P. Koumoutsakos, V. Bontozoglou, An interpretable wildfire spreading model for real-time predictions, *Journal of Computational Science*, under review (2023). [arXiv:2306.01766](https://arxiv.org/abs/2306.01766).
- [12] D. P. Herráez, M. I. A. Sevilla, L. F. Canals, J. M. C. Barbero, A. M. Rodríguez, A GIS-based fire spread simulator integrating a simplified physical wildland fire model and a wind field model, *International Journal of Geographical Information Science* 31 (11) (2017) 2142–2163.
- [13] R. Buerger, E. G. D. Inzunza, P. Mulet, L. M. Villada, Exploring a convection–diffusion–reaction model of the propagation of forest fires: computation of risk maps for heterogeneous environments, *Mathematics* 8 (10) (2020) 1674.
- [14] J. Mandel, L. S. Bennethum, J. D. Beezley, J. L. Coen, C. C. Douglas, M. Kim, A. Vodacek, A wildland fire model with data assimilation, *Mathematics and Computers in Simulation* 79 (3) (2008) 584–606.
- [15] H. P. Hanson, M. M. Bradley, J. E. Bossert, R. R. Linn, L. W. Younker, The potential and promise of physics-based wildfire simulation, *Environmental Science & Policy* 3 (4) (2000) 161–172.
- [16] A. Simeoni, P. A. Santoni, M. Larini, J. H. Balbi, Physical modelling of forest fire spreading through heterogeneous fuel beds, *International Journal of Wildland Fire* 20 (2011) 625–632.
- [17] J. L. Coen, J. D. Beezley, L. S. Bennethum, C. C. Douglas, M. Kim, R. Kremens, J. Mandel, G. Qin, A. Vodacek, A wildland fire dynamic data-driven application system, *11th Symposium on Integrated Observing and Assimilation Systems for the Atmosphere, Oceans, and Land Surface (IOAS-AOLS)* (2007) 3.12.
- [18] R. R. Linn, P. Cunningham, Numerical simulations of grass fires using a coupled atmosphere–fire model: Basic fire behavior and dependence on wind speed, *Journal of Geophysical Research* 110 (1) (2005) D13107.

- [19] J. M. Canfield, R. R. Linn, J. A. Sauer, M. Finney, J. Forthofer, A numerical investigation of the interplay between fireline length, geometry, and rate of spread, *Agricultural and Forest Meteorology* 189-190 (2014) 48–59.
- [20] J. L. Coen, M. Cameron, J. Michalakos, E. G. Patton, P. J. Riggan, K. M. Yedinak, Coupled weather–wildland fire modeling with the weather research and forecasting model, *Journal of Applied Meteorology and Climatology* 52 (1) (2013) 16–38.
- [21] K. Tory, *Models of buoyant plume rise*, Report 451, Melbourne: Bushfire and Natural Hazards CRC (2018).
- [22] D. Morvan, J. Dupuy, Modeling the propagation of a wildfire through a mediterranean shrub using a multiphase formulation, *Combustion and Flame* 138 (3) (2004) 199–210.
- [23] N. P. Lareau, A. Donohoe, M. Roberts, H. Ebrahimian, Tracking Wildfires With Weather Radars, *Journal of Geophysical Research: Atmospheres* 127 (2022) e2021JD036158.
- [24] F. Allaire, V. Mallet, J. B. Filippi, Emulation of wildland fire spread simulation using deep learning, *Neural Networks* 141 (2021) 184–198.
- [25] J. Joshi, R. Sukumar, Improving prediction and assessment of global fires using multilayer neural networks, *Scientific Reports* 11 (2021) 3295.
- [26] D. Shadrin, S. Illarionova, F. Gubanov, K. Evteeva, M. Mironenko, I. Levchunets, R. Belousov, E. Burnaev, Wildfire spreading prediction using multimodal data and deep neural network approach, *Scientific Reports* 14 (2024) 2606.
- [27] M. Ambroz, K. Mikula, M. Frastia, M. Marcis, Parameter estimation for the forest fire propagation model, *Tatra Mountains Mathematical Publications* 72 (2018) 1–22.
- [28] C. Zhang, M. Rochoux, W. Tang, M. Gollner, J.-B. Filippi, A. Trouve, Evaluation of a datadriven wildland fire spread forecast model with spatially-distributed parameter estimation in simulations of the FireFlux I field-scale experiment, *Fire Safety Journal* 91 (2017) 758–767.
- [29] C. Zhang, A. Collin, P. Moireau, A. Trouve, M. Rochoux, State-parameter estimation approach for data-driven wildland fire spread modeling: Application to the 2012 RxCADRE S5 field-scale experiment, *Fire Safety Journal* 105 (2019) 286–299.
- [30] A. Alessandri, P. Bagnerini, M. Gaggero, L. Mantelli, Parameter estimation of fire propagation models using level set methods, *Applied Mathematical Modelling* 92 (2021) 731–747.
- [31] C. Lautenberger, Wildland fire modeling with an Eulerian level set method and automated calibration, *Fire Safety Journal* 62 (2013) 289–298.
- [32] M. C. Rochoux, S. Ricci, D. Lucor, B. Cuenot, A. Trouvé, Towards predictive data-driven simulations of wildfire spread - Part I: Reduced-cost ensemble Kalman filter based on a polynomial chaos surrogate model for parameter estimation, *Natural Hazards and Earth System Sciences* 14 (2014) 2951–2973.
- [33] H. Xue, F. Gu, X. Hu, Data assimilation using sequential Monte Carlo methods in wildfire spread simulation, *ACM Transactions on Modeling and Computer Simulation* 22 (23) (2012) 1–25.
- [34] Z. Lai, C. Mylonas, S. Nagarajaiah, E. Chatzi, Structural identification with physics-informed neural ordinary differential equations, *Journal of Sound and Vibration* 508 (2021) 116196.
- [35] I. E. Lagaris, A. Likas, D. I. Fotiadis, Artificial neural networks for solving ordinary and partial differential equations, *IEEE Transactions on Neural Networks* 9 (5) (1998) 987–1000.
- [36] M. Raissi, P. Perdikaris, G. E. Karniadakis, Physics-informed neural networks: A deep learning framework for solving forward and inverse problems involving nonlinear partial differential equations, *Journal of Computational Physics* 378 (2018) 686–707.
- [37] G. Karniadakis, Y. Kevrekidis, L. Lu, P. Perdikaris, S. Wang, L. Yang, Physics-informed machine learning, *Nature Reviews Physics* 3 (2021) 422–440.
- [38] K. Hornik, M. Stinchcombe, H. White, Multilayer feedforward networks are universal approximators, *Neural networks* 2 (5) (1989) 359–366.
- [39] A. L. Sullivan, Wildland surface fire spread modelling, 1990–2007. 1: Physical and quasi-physical models, *International Journal of Wildland Fire* 18 (4) (2009) 349–368.

- [40] I. N. Harman, J. J. Finnigan, A simple unified theory for flow in the canopy and roughness sublayer, *Boundary-Layer Meteorology* 123 (2007) 339–363.
- [41] M. A. Finney, J. D. Cohen, I. C. Grenfell, K. M. Yedinak, An examination of fire spread thresholds in discontinuous fuel beds, *International Journal of Wildland Fire* 19 (2010) 163–170.
- [42] M. A. Finney, J. D. Cohen, J. M. Forthofer, S. S. McAllister, M. J. Gollnerb, D. J. Gorbamb, K. Saito, N. K. Akafuah, B. A. Adams, J. D. English, Role of buoyant flame dynamics in wildfire spread, *Proceedings of the National Academy of Sciences (PNAS)* 112 (32) (2015) 9833–9838.
- [43] F. J. Seron, D. Gutierrez, J. Magallon, L. Ferragut, M. I. Asensio, The evolution of a WILDLAND forest FIRE FRONT, *The Visual Computer* 21 (2005) 152–169.
- [44] A. L. Sullivan, Inside the inferno: Fundamental processes of wildland fire behaviour. Part 1: Combustion chemistry and energy release, *Current Forestry Reports* 3 (2017) 132–149.
- [45] D. R. Sudhakar, A. K. Kolar, Experimental investigation of the effect of initial fuel particle shape, size and bed temperature on devolatilization of single wood particle in a hot fluidized bed, *Journal of Analytical and Applied Pyrolysis* 92 (1) (2011) 239–249.
- [46] B. Leckner, K. M. Hansson, C. Tullin, A. V. Borodulya, V. I. Dikalenko, G. I. Palchonok, Kinetics of fluidized bed combustion of wood pellets, in: R. B. Reuther (Ed.), *Proc. 15th International Conference on Fluidized Bed Combustion*, Savannah, GA, US, 1999, pp. 15, Paper FBC99.0047.
- [47] N. McCarthy, A. Guyot, A. Dowdy, H. McGowan, Wildfire and weather radar: A review, *Journal of Geophysical Research: Atmospheres* 124 (2019) 266–286.
- [48] R. M. Nelson, Re-analysis of wind and slope effects on flame characteristics of mediterranean shrub fires, *International Journal of Wildland Fire* 24 (2011) 1001–1007.
- [49] E. L. Cussler, *Diffusion: Mass Transfer in Fluid Systems*, 3rd Edition, Cambridge University Press, Cambridge, U.K., 2009.
- [50] N. P. Cheney, J. S. Gould, Fire growth in grassland fuels, *International Journal of Wildland Fire* 5 (4) (1995) 237–247.
- [51] E. Inoue, On the turbulent structure of air flow within crop canopies, *Journal of the Meteorological Society of Japan* 41 (6) (1963) 317–326.
- [52] J. M. Forthofer, B. W. Butler, N. S. Wagenbrenner, A comparison of three approaches for simulating fine-scale surface winds in support of wildland fire management. Part I. Model formulation and comparison against measurements, *International Journal of Wildland Fire* 23 (2014) 969–981.
- [53] M. P. Murgai, H. W. Emmons, Natural convection above fires, *Journal of Fluid Mechanics* 8 (4) (1960) 611–624.
- [54] A. Baydin, B. Pearlmutter, A. Radul, J. Siskind, Automatic differentiation in machine learning: A survey, *Journal of Machine Learning Research* 18 (2018) 1–43.
- [55] D. E. Rumelhart, G. E. Hinton, R. J. Williams, Learning representations by back-propagating errors, *Nature* 323 (1986) 533–536.
- [56] H. Robbins, S. Monro, A stochastic approximation method, *Annals of Mathematical Statistics* 22 (3) (1951) 400–407.
- [57] D. P. Kingma, J. Ba, Adam: A method for Stochastic Optimization, *CoRR abs/1412.6980* (2014).
- [58] R. H. Byrd, P. Lu, J. Nocedal, C. Zhu, A limited memory algorithm for bound constrained optimization, *SIAM Journal on Scientific Computing* 16 (5) (1995) 1190–1208.
- [59] G. Cybenko, Approximation by superpositions of a sigmoidal function, *Mathematics of Control, Signals, and Systems* 2 (4) (1989) 303–314.
- [60] K. Funahashi, On the Approximate Realization of Continuous Mappings by Neural Networks, *Neural Networks* 2 (1989) 183–192.
- [61] M. Leshno, V. Y. Lin, A. Pinkus, S. Schocken, Multilayer Feed- forward Networks with a Nonpolynomial Activation Function can Approximate any Function, *Neural Networks* 6 (1989) 861–867.

- [62] D. Silver, J. Schrittwieser, K. Simonyan, I. Antonoglou, A. Huang, A. Guez, T. Hubert, L. Baker, M. Lai, A. Bolton, Y. Chen, Mastering the Game of Go Without Human Knowledge, *Nature* 550 (2017) 354–359.
- [63] J. Yu, L. Lu, X. Meng, G. E. Karniadakis, Gradient-enhanced physics-informed neural networks for forward and inverse PDE problems, *Computer Methods in Applied Mechanics and Engineering* 393 (2022) 114823.
- [64] L. Lu, X. Meng, Z. Mao, G. Karniadakis, Deepxde: A deep learning library for solving differential equations, *SIAM Rev.* 63 (2021) 208–228.